



Resolution Enhancement by Variable Zoom Trajectory in X-Ray Computed Tomography

Pavel Blažek^{1,2,3} · Alexander Suppes¹ · Dominik Wolfschläger² · Tomáš Zikmund³ · Jozef Kaiser³ · Robert H. Schmitt^{2,4}

Received: 30 January 2024 / Accepted: 6 May 2024 / Published online: 4 July 2024
© The Author(s) 2024

Abstract

Flat objects like electronic boards are challenging samples for high-resolution X-ray computed tomography scanning because their largest dimension significantly limits the magnification using circular trajectory scans. One way to improve spatial resolution for such samples is to utilize variable zoom trajectory. During variable zoom trajectory scanning, the source-to-object distance changes during the 360° rotation to maximize the magnification in the projections. Here, we propose an automatic variable zoom trajectory generation algorithm for arbitrary object and region of interest (ROI). We analyze how such a trajectory can enhance resolution in different cases and how isotropic is the resolution in the reconstructed volume. We demonstrate that the resolution can be improved without destroying the sample. However, the improvement is manifested mainly in directions in which we achieved the highest magnification in the projection.

Keywords Variable zoom · Trajectory · X-ray computed tomography · Resolution · MTF

1 Introduction

X-ray computed tomography (CT) emerged as an efficient tool for comprehensive 3D inspection of various types of samples. Due to its ability to analyze both inner and outer features of objects with high resolution down to micron and submicron scale, it has become an essential technology for non-destructive inspection of defects in various industrial fields as well as in the scientific domain. For example, Li-Ion batteries may contain various types of defects such as impurities in the cathode and anode, overhangs, or delamination which reduce the battery performance and contribute to rapid aging [1, 2]. Also, other electronic parts may suffer from defects such as voids in solder joints which may lead to component failure [3–6].

Challenges appear when scanning complex samples of large dimensions which are difficult to fit into field of view (FOV) of CT scanner. Even if focusing only on part of the object with region of interest (ROI) scanning, available magnification and therefore spatial resolution can be limited when using standard circular trajectory, because the object could collide with CT system components, or the ROI is still too large to fit in the detector under desired magnification. For example, when scanning objects of cylindrical shape and high aspect ratio, users can decide to move the sample closer to the source to increase magnification and the resulting resolution. However only part of the sample will be scanned. Fitting the whole object in the detector FOV could on the other side decrease the resolution. Other example of challenging object are those of planar shape like electronic boards, pouch battery cells, or composite plates, which are often analyzed for the presence of various defects [7–9]. Several techniques were already proposed to increase resolution and extend the scanning FOV in both longitudinal and lateral directions, however, their applicability depends on the overall object dimensions, position and dimension of the ROI, CT scanner's geometry and the available degrees of freedom during acquisition.

The FOV can be extended longitudinally by stitching multiple circular scans [10], employing helical trajectory

✉ Pavel Blažek
pavel.blazek@bakerhughes.com

¹ Baker Hughes Digital Solutions GmbH, Wunstorf, Germany

² WZL | RWTH Aachen University, Aachen, Germany

³ Central European Institute of Technology, Brno University of Technology, Brno, Czech Republic

⁴ Fraunhofer Institute for Production Technology IPT, Aachen, Germany

CT or similar trajectories like ellipse-line-ellipse [11–13]. Such techniques can be used to improve the resolution and image quality of CT scans for samples like cylindrical batteries or additive manufactured components while acquiring data for the whole ROI [14, 15]. To extend the FOV laterally and improve resolution, a detector offset can be used [16–18]. However, in many scenarios, such as analyzing defects in parts of large flat objects as electronic circuit boards, the resolution is limited mainly by the smallest achievable source-to-object distance (SOD) instead of the detector size. The sample cannot be moved close enough to the source to reach the geometrical magnification necessary for the required resolution, because the flat object would collide with the tube during 360° rotation. In such cases, limited angle tomography, laminography or tomosynthesis techniques could be used to avoid collision while utilizing higher geometrical magnification. These approaches may enhance the resolution but will lead to image artifacts due to incomplete information from some angles [19, 20]. Missing data in these types of scans can be completed by combining multiple scans with different trajectories or magnifications as proposed in [21], which may however lead to a significant increase in time costs for the whole measurement.

It is also possible to obtain projection data from all directions in a single scan and increase the information gain by changing the SOD during the object rotation to avoid collisions and increase the magnification in some of the projections. An elliptical trajectory was proposed in medical CT to allow closer following of the contours of the human body, but the effects were tested only on small simulated dataset of 64 projections and did not focus on evaluation of resolution improvement [22]. Dabravolski et al. [23] proposed moving the object as close as possible to the source for each projection while avoiding truncation of the whole object's projection by detector edges. They computed variable zoom trajectory for a piece of pencil using an outer hull estimated from a circular CT scan reconstruction as an input and demonstrated that slightly higher level of detail can be achieved. Their study was however limited to only one real experiment with subjective evaluation of results. Proposed algorithm also does not consider focusing only on a part of an object (ROI). Nikishkov et al. [24] applied a variable zoom technique together with a modified Feldkamp-Davis-Kress (FDK) reconstruction algorithm to improve resolution of ROI (impact area with defects) in composite plates. They used an analytical formula to generate the trajectory using information about sample width and length and included the safety offset defined by a user. The formula was however derived assuming rectangular object and ROI in object's center. It could therefore lead to unnecessary low magnification in projection from some angles in case of more complex shape and position of an object and an ROI. The performance was evaluated by measuring the sharpness of the material interface, dimensions

of holes and attached wires showing improvement over conventional circular CT. Sharpness improvement was shown as well in the reconstruction of the composite plates, although part of the projections was acquired with lower magnification. Some manufacturers of CT systems offer an option to acquire data with variable zoom trajectory, determined from the user-specified boundary of the object and position of ROI [25].

In this work, we present an automatic algorithm for generating variable zoom trajectory for arbitrary position and shape of object and ROI inside to maximize magnification in each projection. We demonstrate the improvement of resolution on two realistic samples and two reference objects. Due to their flat and elongated shape, the realistic samples – printed circuit board (PCB) with a BGA (ball grid array) and rectangular prismatic cell – present a challenge for conventional circular CT measurement when high resolution is required in ROIs. They are therefore suitable for scanning with variable zoom trajectory. Because the magnification in projection is higher from some angles in variable zoom acquisition, we expect that the resulting quality and resolution have directional dependency in the reconstructed data. We quantify the anisotropic spatial resolution using modular transfer function (MTF) calculated from CT data of a precision ruby sphere, and interpolated spatial resolution (iSR_{CT}) values obtained using a bar pattern phantom.

2 Methods

2.1 Samples

In this study, we inspected two flat samples suitable for variable zoom CT inspection. The first sample was a PCB with overall approximate dimensions of $10 \times 16 \text{ mm}^2$. Our focus in this object was on a ball grid BGA, a common subject of interest for CT inspection to detect defects in the solder joint, such as bridges, voids or missing connections [6]. Due to the position of the BGA within the circuit board, we could measure it at an angle of approximately 45°. This not only reduced the penetration length but also increased the possible magnification. However, the smallest achievable SOD was around 100 mm, which can limit defect detection.

The second sample used in our study was a prismatic cell with an aluminum casing and approximate dimensions of $11 \times 22 \text{ mm}^2$. In this case, we analyzed the region in the corner of the electrode stack to investigate its structure. Similar to the previous sample, the cell was tilted to approximately 45 degrees, enabling us to use a circular trajectory at the highest magnification with a SOD of 90 mm. In both cases, the region of interest (ROI) had a diameter of 16 mm.

For evaluating the resolution improvement, we employed two reference objects. The first one was the micro-CT bar

pattern phantom (QRM, Möhrendorf Germany) [4] which offered straightforward visualization of the resolution in terms of line pairs along two axes. The second reference object was a ruby sphere with a diameter of 10 mm. We utilized this sphere to evaluate the Modulation Transfer Function (MTF) in different directions based on the procedure described in standard ASTM 1695–95 [5].

It is essential to acknowledge that resolution may differ depending on various material interfaces, and multiple factors can impact its determination. Consequently, the quantification of resolution derived from our reference objects (ruby/air and silicon/resin interfaces) cannot be directly transferred to the measurements of PCB (solder/air interface for defects in BGA) or prismatic cell (consisting of multiple materials: Al/Cu current collectors, polymer separators, cathode and anode, air, etc.)

2.2 Trajectory Generation

Goal of our variable zoom trajectory generator is to maximize magnification in each projection by moving sample as close as possible to the source, while the projection of ROI is not laterally truncated by the detector and sample does not collide with CT system components. Our algorithm uses CT system geometry specifications (detector width and source-to-detector distance), object specification (width and length in cross-section), ROI specification (dimensions and position in the object), and safety distance for collision avoidance as an input. Information about object and ROI can be input as a CAD model or from manual measurement by a user. Here we did not have the CAD model from the manufacturer of the PCB and cell, so we measured the object and included a safety distance (D_S) to create a simplified cuboid model that represents the object’s outer hull. D_S can be set by operator to ensure safety of acquisition and should therefore consider at least possible misalignment of an object from model position and depth of focal spot in the tube. Additionally, we determined the position and size of ROI in the model representation. The sample is positioned on the stage with a rotating axis going through the center of the ROI.

In this work we simplified the geometry to 2D, such as in fan beam CT which was sufficient to demonstrate significant improvement of resolution. We assume standard aligned geometry with source and center of detector lying at “zoom”

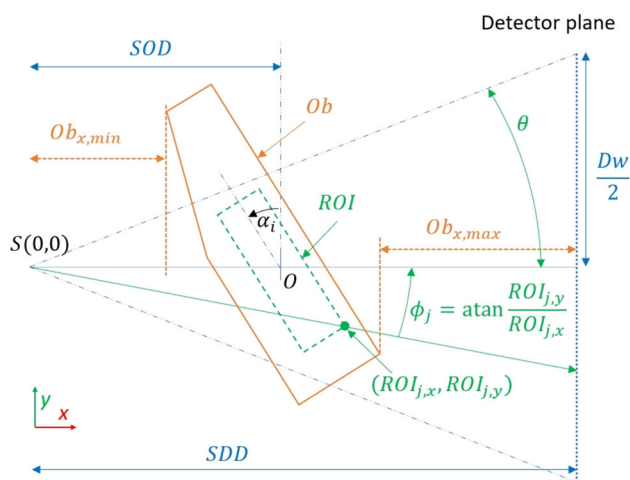


Fig. 1 Depiction of geometry used for trajectory generation

axis x as depicted in Fig. 1. Detector’s plane is perpendicular to axis x and its collums are parallel to rotation axis O of the object, which is parallel of axis z . Source can be described as a point lying in the origin of global coordinate system $S = (0,0)$. Detector is represented with corner points $D_1 = (SDD, \frac{Dw}{2})$, $D_2 = (SDD, -\frac{Dw}{2})$. Object and ROI are represented as set of points $Ob = \{(Ob_{i,x}, Ob_{i,y}), \dots\}$ and $ROI = \{(ROI_{i,x}, ROI_{i,y}), \dots\}$ whose coordinates depend on object rotation angle α and SOD . During the acquisition, object is rotating through angle α around axis O , usually positioned in the center of ROI and they are shifting with varying SOD . Under these assumptions, the trajectory of a variable zoom CT scan is described as a set of (α, SOD) pairs.

To determine set of optimal SODs, we need to evaluate two conditions. First, the object cannot collide with CT system components, in our case, the object does not crash with the source or the detector. This is done by iterating through x coordinates of all points of Ob and checking whether the maximal x coordinate of object is not higher than SDD and minimal x coordinate of the object is not lower than 0. Secondly, we need to ensure that the ROI projection is covering whole FOV and is not truncated by the detector. This is done by finding a point of ROI corresponding to maximal angle of $\phi_i = \text{atan} \frac{ROI_{i,y}}{ROI_{i,x}}$, which should be in optimal position equal to half of cone-angle ($\theta = \text{atan} \frac{Dw}{2SDD}$).

Algorithm 1 Generation of variable zoom trajectory

SDD, Dw	Information about scanning geometry
$Ob = \{Ob_1, \dots, Ob_N\}$	
$ROI = \{ROI_1, \dots, ROI_M\}$	Initial position, with O at $S(0,0)$, so $SOD = 0$
$\alpha = \{\alpha_1, \dots, \alpha_{\#P}\}$	Set of projection angles
$SODs = \{SOD_1, \dots, SOD_{\#P}\}$	Set of SODs, output
For all $\alpha_i \in \alpha$:	Iterate through all projection positions
Rotate Ob and ROI to angle α around O	Coordinate transform of all Ob and ROI
For SOD from 0 to SDD :	
Shift Ob and ROI to SOD	Coordinate transform of all Ob and ROI
If \min of all $Ob_{x,j} \leq 0$:	
Continue to the next iteration	Object collides with the source
End If	
If \max of all $ \phi_j \geq \theta$	
Continue to the next iteration	ROI is out of FOV
End If	
Break the loop	Found SOD where ROI is in FOV, and object does not collide
End For	
If \max of all $Ob_{x,j} \geq SDD$	Check if object collides with the detector
Raise error	Object does not fit in the CT system
$SOD_i = SOD$	
End For	
Return $SODs$	

2.3 CT Measurements

All CT scans were acquired using micro-CT Phoenix Vtomelx M300 (Waygate Technologies, Wunstorf, Germany) equipped with a flat panel detector of pixel size $200 \mu\text{m}$ and resolution of 2024×2024 pixels². A summary of measurement parameters is shown in Table 1. The PCB was measured first with a conventional circular trajectory (CLR) with $SOD = 103.1$ mm set to avoid the risk of collision between the measured object and the X-ray tube, which resulted in a relatively low-resolution reconstruction. Subsequently, we optimized the trajectory using a variable zoom algorithm (VZM trajectory) and acquired another scan. Furthermore, we generated another variable zoom trajectory (VZE) by moving the ROI in the sample model more to the side, and generated also circular trajectory (CHR) with the smallest SOD used during the VZM trajectory ($SOD = 28.3$ mm). This would however require cutting the ROI from the PCB, so this scan could not be performed in this case and the SOD is applied only for scanning our reference objects. We needed to adjust beam energy for scanning the bar pattern phantom and ruby sphere, however, we kept the tube power at the same value to reduce the effect of different spot sizes on resolution measurement. We also measured the prismatic cell with a circular trajectory (CLR2) and generated a variable zoom trajectory with a focus on an ROI at the corner of the electrode stack (VZM2). All trajectories applied in this work are shown in Fig. 2

In each measurement, 2300 projections were acquired over 360° rotation of the sample. The beam parameters and filtering were adjusted for each sample. To avoid the effect of varying unsharpness due to different spot sizes we adjusted the tube current so that the beam power remained the same for both the PCB and the reference object measurements. This allowed us to separate the influence of the used trajectory from the effect of other parameters.

The reconstruction was performed by Phoenix Dataslx software (Waygate Technologies, Wunstorf, Germany), which uses a modified FDK algorithm to accommodate variable zoom geometry. The acquisitions from all trajectories were reconstructed with the same voxel size of $7.3 \mu\text{m}$ (PCB, bar pattern, ruby sphere) and $8.3 \mu\text{m}$ (prismatic cell).

2.4 Resolution Evaluation

The ASTM 1695-95 [26] describes a procedure for calculating MTF from one tomographic cross-section of a cylinder or a sphere. First, the edge profile is generated from points around the sphere edge to obtain the edge response function (ERF). The point spread function (PSF) is then determined as a derivative of ERF. Finally, the MTF is obtained by calculating the amplitude of the Fourier transform of the PSF and normalization. To evaluate the directional dependency of MTF in the CT data we modified this approach and used only part of the circumference to generate ERF. For each dataset, the sphere cross-section was split in four quarters as shown in Fig. 3.

Table 1 CT measurement parameters

Sample	PCB	Prismatic cell	MicroCT Bar Pattern	Ruby sphere
N. of projections	2300	2300	2300	2300
Voltage/kV	240	200	160	160
Tube power/W	7.2	8	7.2	7.2
Filter/mm	0.5 Sn	0.5 Cu	0.1 Cu	0.1 Cu
SDD/mm	775	775	775	775
Trajectories (SOD range in mm)	VZM (28.3–103.1) CLR (103.1)	VZM2 (32.3–83.0) CLR2 (90)	VZM (28.3–103.1) VZE (28.3–152.1) CHR (28.3) CLR (103.1)	VZM (28.3–103.1) VZE (28.3–152.1) CHR (28.3) CLR (103.1)
Voxel size/ μm	7.3	8.3	7.3	7.3

Source trajectory around a fixed object

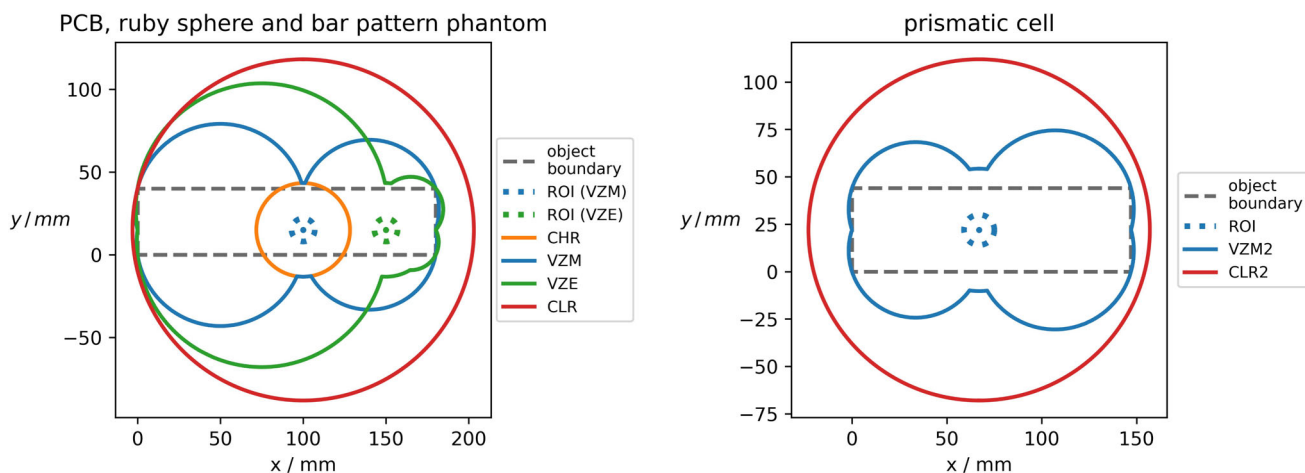


Fig. 2 Trajectories used in this study. Here shown from perspective of fixed object and ROI and moving X-ray source. Left: variable zoom trajectories based on PCB sample and two ROIs (VZM, VZE) and high

and low resolution conventional circular trajectory (CLR, CHR). Right: trajectory used with prismatic cell sample

In the case of ROI located in the middle of flat objects and scanning with the variable zoom trajectory (here VZM trajectory), some parts of the edge are reconstructed using information from higher magnification projections (Q1 and Q3), while other parts are reconstructed using lower magnification projections (Q2 and Q4). We anticipate that this difference will result in disparities in calculated MTF values between these regions of the sphere. Furthermore, we will assess the $MTF_{10\%}$ value, i.e., the frequency at 10% modulation, for comparison as well.

We also used a QRM micro-CT bar pattern with grooves in two perpendicular directions and holes. This allows straightforward visualization of resolution while allows also quantitative evaluation. We analyzed results using a procedure based on standard ASTM 2576 [27]. In each line

pattern, we measured the line profile averaging over a width of approximately 60% of the lines. In each dataset, four-line patterns were evaluated in each direction. The interpolated spatial resolution is then calculated from the second-order polynomial approximation of the dip vs. the line pair spacing as the 20% dip value. In cases where a measurement of line pairs with an average dip of less than 20% was not possible, we used the value of the next line pattern with zero dip as the iSR_{CT} . We will calculate two values $iSR_{CT,x}$ and $iSR_{CT,y}$ corresponding to the resolution from line patterns in two directions.

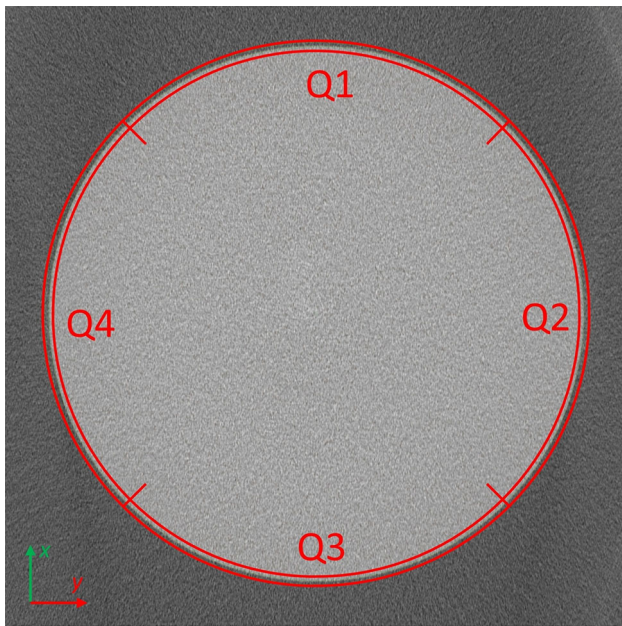


Fig. 3 Tomographic cross section of the sphere used for determination of MTF. Division into 4 sectors

3 Results and Discussion

A typical task for the analysis of the PCB used in this study is defect detection in BGA and in copper tracks through the board. Using a conventional circular scan, we were able to measure the board with $SOD = 103$ mm (CLR), corresponding to $7.5 \times$ magnification, while the SOD for the variable zoom acquisition (VZM) varied from 28.3 to 103 mm increasing the magnification up to 27. Even with the circular trajectory, we were able to reveal many defects in the solder balls. Increasing magnification during the variable zoom scan led to improvement of resolution of these defects as is shown in Fig. 4. The improvement is demonstrated in the details of three selected defects (Fig. 5). The smallest of the selected defects (a) has dimensions of approximately $60 \times 30 \times 50 \mu\text{m}^3$. In the CLR, the defect is barely visible to a human observer. It is possible to distinguish a dip in a gray value line profile over the defect cross-section, but due to blurring its width appears two times larger than in the VZE scan. VZE trajectory also improved the sharpness of the copper track on the board, however, no notable defects were found (Fig. 4f, g).

With conventional circular trajectory, we achieved $9 \times$ magnification, while with the variable zoom trajectory the magnification in projections reached up to 24. In the circular scan we were able to distinguish layers of cathode, anode, copper current collector in anode (Fig. 6c), and some polymer separators (Fig. 6a). With the VZE2 trajectory, we observe a higher-resolved polymer separator (Fig. 6b) and we are also able to resolve the aluminum current collector inside

the cathode, as it can be seen in the gray value line profiles in Fig. 6.

Although the prismatic cell and PCB scans showed improvement by variable zoom trajectory, the evaluation is to some extent subjective, and it is difficult to quantify it on those samples. Therefore, we conducted a quantitative evaluation using two reference objects. We used the object parameters of the PCB and generated a circular trajectory with the smallest and highest SODs used in the VZM trajectory (CLR and CHR trajectory) and we also generated a variable zoom trajectory for ROI positioned closer to the edge of the sample (VZE). We applied these four trajectories for scanning the bar pattern and ruby sphere phantoms.

CT reconstructions of bar pattern phantom are visualized in Fig. 7. With the CLR trajectory, we can barely distinguish line patterns of $30 \mu\text{m}$ width, while with the VZM trajectory we can distinguish patterns down to $10 \mu\text{m}$ in y-direction oriented patterns or $20 \mu\text{m}$ in the x-direction. We quantitatively evaluated the contrast dips in the line profile through patterns which resulted in $iSR_{CT,x} = 29 \mu\text{m}$ and $iSR_{CT,y} = 25 \mu\text{m}$ for CLR scan, while with the VZM trajectory, the resolution was improved to $iSR_{CT,x} = 21 \mu\text{m}$ and $iSR_{CT,y} = 5 \mu\text{m}$ (Table 2). In this case, the line patterns in the y-direction are reconstructed using projections collected with higher magnification (up to $27 \times$) while in the x-direction the magnification is lower (down to $7.5 \times$) leading to the anisotropy in resolution. The situation is different when the ROI is positioned more to the edge of the object such as in the case of VZE trajectory. Here we can obtain more than 180° rotation with high magnification projections which leads to even more improvement in resolution in x-direction where $iSR_{CT,x} = 5 \mu\text{m}$. This makes the resolution from the VTE scan reach almost to level in the high-resolution circular scan although we can still observe lower resolution on the x-direction $10 \mu\text{m}$ pattern. It is visible also in the dip measurement (Fig. 8) which is 65% for CHR trajectory, 57% for VZE in the y-direction but only 39% for VZE in the x-direction and 44% for VZM in the y-direction, while for VZM in x-direction the $10 \mu\text{m}$ pattern could not be measured at all.

We also analyzed the performance of different trajectories by evaluating the MTF on ruby sphere measurement and calculated its 10% frequency to characterize the resolution. MTF charts are shown in Fig. 9 and $MTF_{10\%}$ values in Fig. 10 and Table 3. The highest resolution was achieved with CHR trajectory which led to $MTF_{10\%}$ from 78 and 82 lp/mm. As the phantom was measured relatively close to the source, we observed an edge enhancement effect. It is assumed to be caused by phase contrast, leading to enhanced contrast in structures of certain sizes which is demonstrated in the MTF as a maximum at higher frequency instead of at zero as in other cases. The lowest resolution was obtained with the CLR scan leading to $MTF_{10\%} = 23$ lp/mm. Both variable

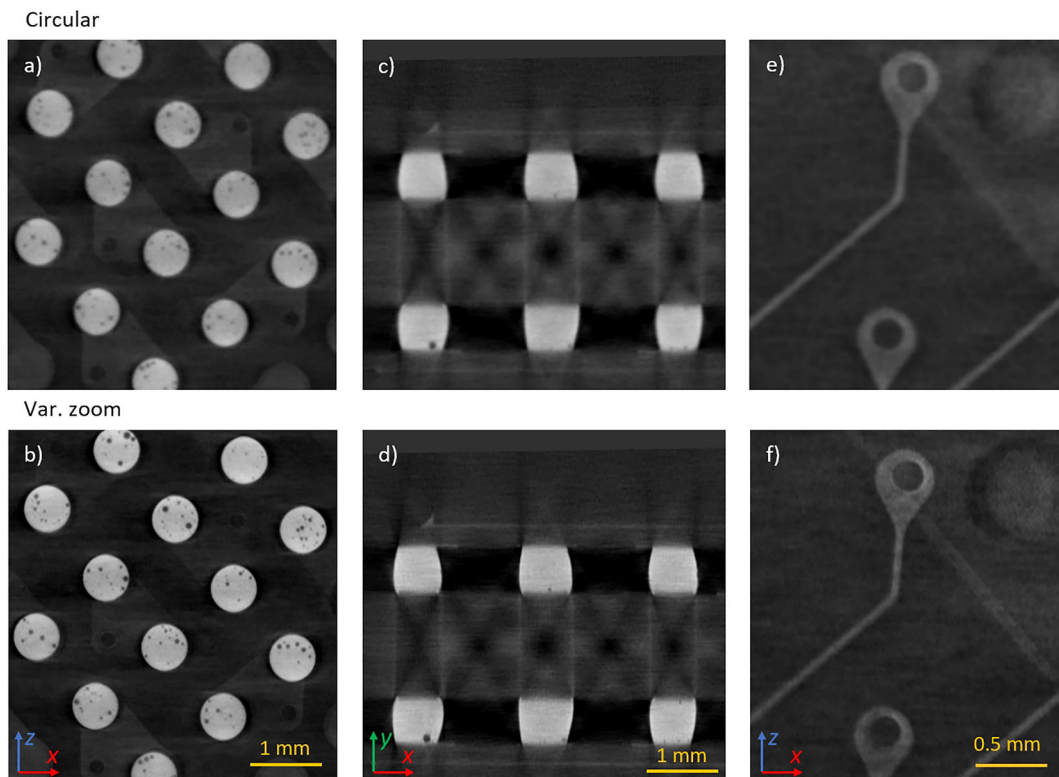
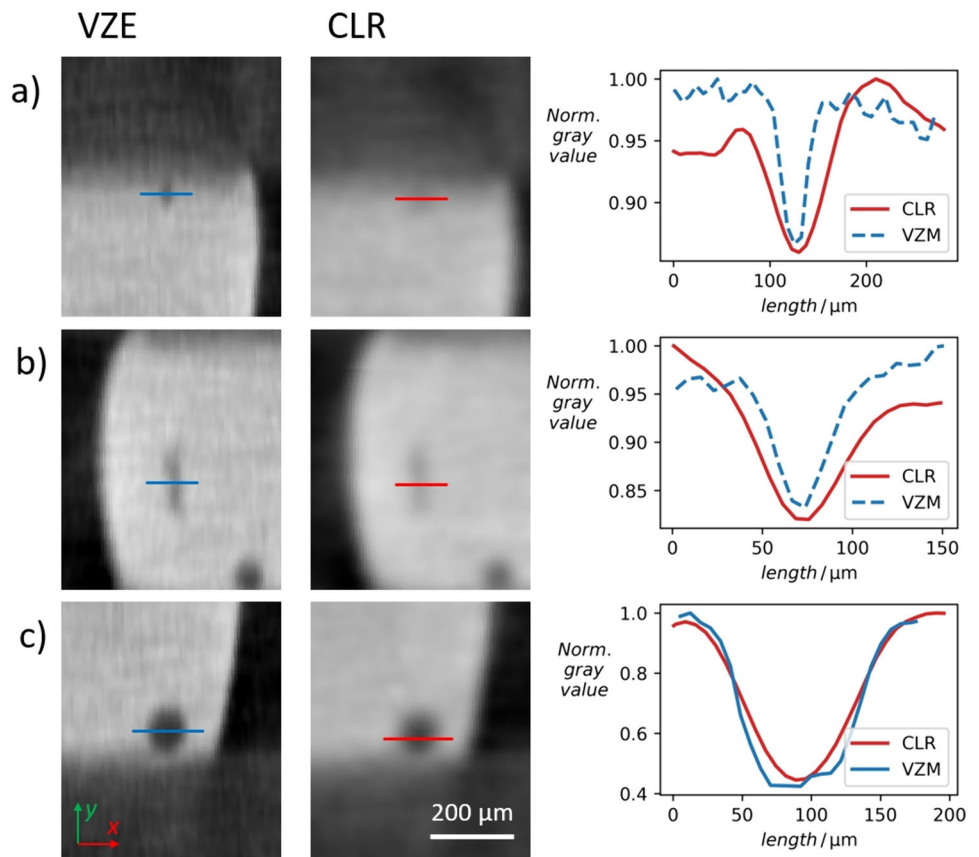


Fig. 4 Tomographic cross-section of PCB. Top row show results from circular scan, bottom row shows results from variable zoom scan. **a, b** Cross-section through zx-plane. **c, d** Cross-section through the yx-plane. **e, f** Detail of copper tracks

Fig. 5 Details of three defects in PCB sample, comparison of VZE and CLR scan. Visualization of normalized gray value line-profiles over defects



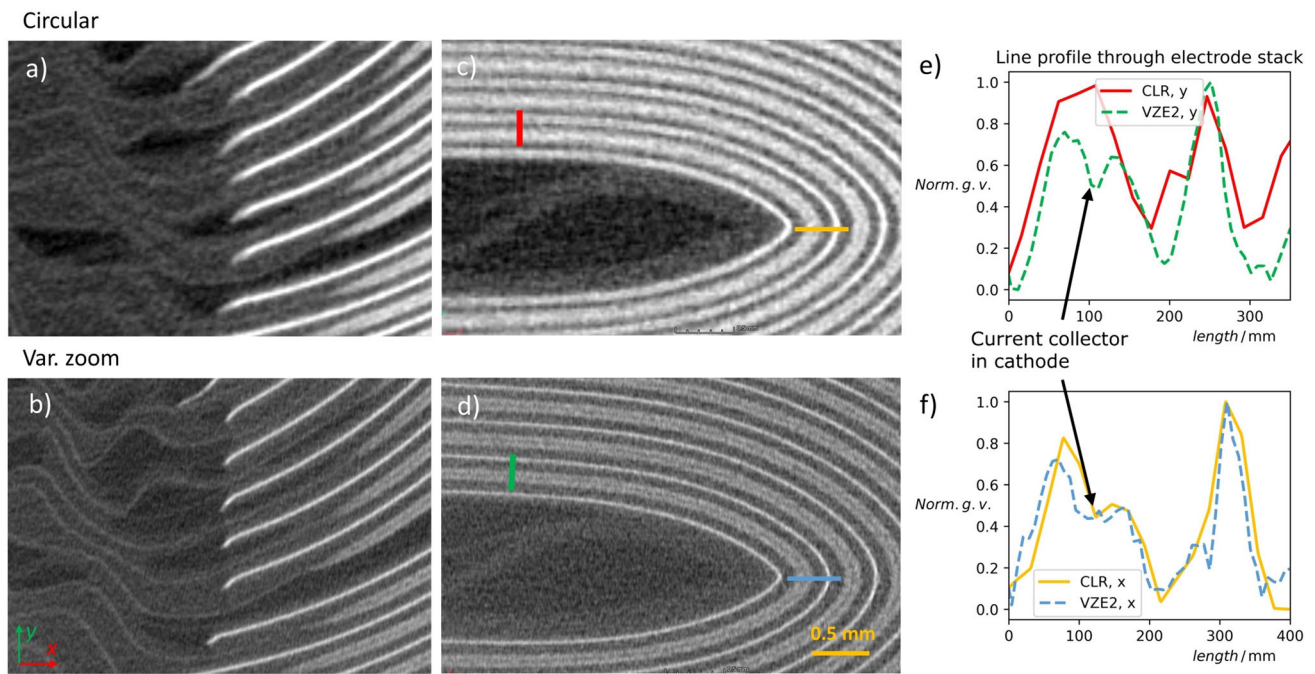
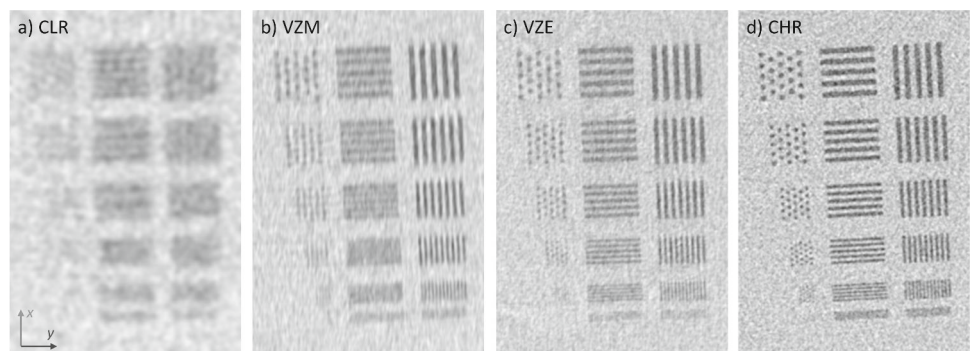


Fig. 6 Tomographic cross-section of prismatic cell. Top row images are showing the circular scan results, bottom row variable zoom results. **a**, **b** show detail of the end of the electrode stack with separators, **c**, **d** is detail of the center of the cathode stack. Lines are showing position of

line profiles which are plotted in the charts **e**, **f** of normalized gray value with same colors. Arrows point to the dip corresponding to Al current collector in cathode

Fig. 7 Tomographic cross-sections from bar pattern phantom scans. Detail with line and point patterns with width of 30, 25, 20, 15, 10 and 5 μm (from top to bottom). **a** CLR, **b** VZM, **c** VZE, **d** CHR



zoom scans showed improvements in resolution compared to the CLR scan. In the VZM scan the $\text{MTF}_{10\%}$ reached up to 56 lp/mm in Q4 and 39 lp/mm in Q2, while in Q1 and Q3 the $\text{MTF}_{10\%}$ was comparably lower with 28 lp/mm. Again, it showed an anisotropy due to varying magnification in this trajectory. An even higher resolution was achieved with VZE trajectory leading to $\text{MTF}_{10\%}$ from 54 to 69 lp/mm, demonstrating a lower difference of resolution in different directions due to a larger portion of projections being acquired with similar magnification.

We point out that although the MTF is obtained by evaluating a large number of pixels around the sphere circumference or in our case its sections, it still can be sensitive to image noise and other influencing factors during measurement. The

MTF for both the Q4 and Q2 sections of the VZM scan has a similar shape, however, it is getting almost monotonous around 10% value which leads to a significant difference (more than 25%) in the $\text{MTF}_{10\%}$ values. Common practice is to use this method for performance checks of CT systems to allow for the optimization of acquisition parameters and higher tube power during the measurement which reduces the noise. Here, we reduced the power to keep the spot size small enough to avoid blurring in the projected image, which would neglect the resolution gained by using higher magnification. Similarly, the evaluation of the bar pattern phantom was more challenging due to relatively noisy CT data. ASTM E2576 is designed for the characterization of detectors from radiographs. These can be more easily optimized to reduce noise

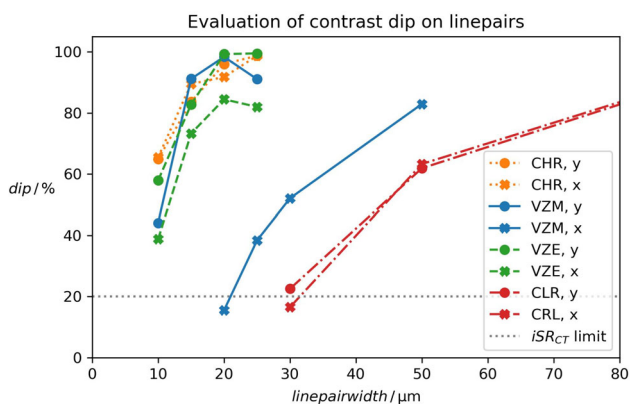


Fig. 8 Average dip in each line pattern from variable zoom dataset. Measurement values for 100 μm and 150 μm line-patterns from CRL trajectory measurement were cropped

Table 2 Evaluation of iSR_{CT} on bar pattern phantom for two variable zoom and two circular trajectories in two perpendicular directions

Trajectory	$iSR_{CT,x} / \mu\text{m}$	$iSR_{CT,y} / \mu\text{m}$
VZM	21	5
VZE	5	5
CHR	5	5
CLR	29	25

by increasing exposure and averaging, which would however need to be multiplied by a number of projections used in CT scans and therefore require significantly higher time costs for CT data evaluation. Also commonly used duplex-wire type IQIs [28] use wire pairs with smaller steps between the width of different patterns, it is therefore easier to satisfy

the recommendation to measure two line pairs under 20% dip to obtain the reliable value of iSR . We could not satisfy this recommendation in any of our measurements as the bar pattern used in our experiments contained line patterns in the measured range with 5 μm steps. This resulted in iSR_{CT} values of 5 μm, which were the closest line patterns with zero measured dip, but these values are also less than utilized voxel size. It would be beneficial to use a phantom with smaller steps between line-pair widths to be able to capture more realistic values, which in this case would probably lie between 5 and 10 μm.

All our measurements used the same total number of projections (2300) to avoid number of projections as a possible influence factor. This number was selected according to the manufacturer’s recommendation for the CHR scan. For the CLR scans with lower magnification and ROI covering a smaller portion of the detector, we however could per the manufacturer’s recommendation use a lower number of projections without significant resolution loss. We can therefore assume that the number of projections or more specifically the sampling angle between projections could be also adjusted in variable zoom scans to reduce the time cost. However, no specific recommendations for this type of trajectory exist in current literature according to our knowledge and it is therefore a suitable topic for future research. In our algorithm we also considered only simplified 2D geometry of the CT system and object. It was sufficient to demonstrate capabilities of the variable zoom trajectory, but the improvement could be made to consider 3D shape of the object and shape and real time position of CT system components, leading to more robust collision protection and to even better resolution.

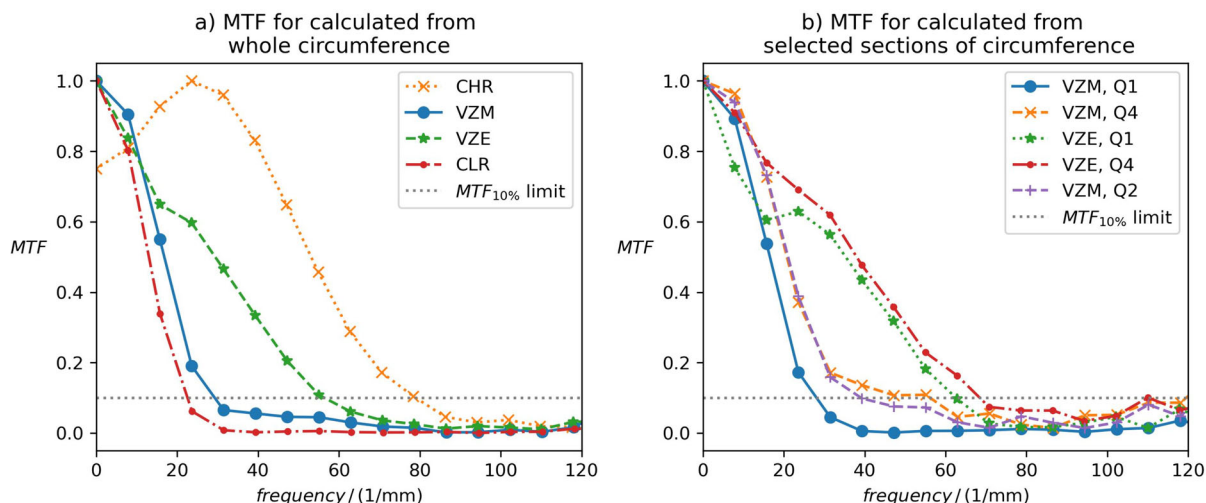


Fig. 9 MTF calculated from ruby sphere reconstructions. **a** Calculation from whole circumference for all trajectories applied. **b** Calculation for sectors Q1 (where we assume lower resolution) and Q4 (where we assume lower resolution) for two variable zoom trajectories applied

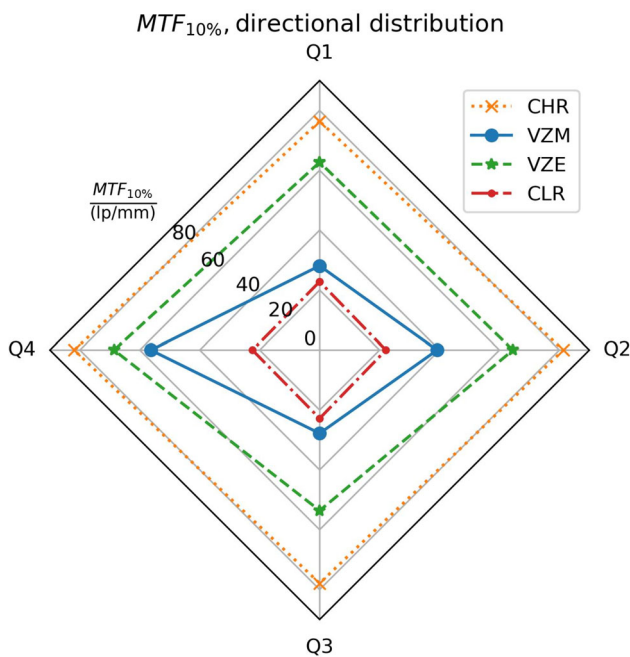


Fig. 10 $MTF_{10\%}$ evaluation and directional distribution for variable zoom and circular trajectories

Table 3 $MTF_{10\%}$ evaluation and directional distribution for variable zoom and circular trajectories

Region	$MTF_{10\%} / (lp/mm)$			
	CHR	VZM	VZE	CLR
Whole circumference	79.1	29.3	57.3	22.6
Q1	76.4	28.1	62.7	22.8
Q2	81.3	39.2	64.5	22.1
Q3	77.9	27.8	53.6	22.8
Q4	81.9	56.3	68.6	22.4

4 Conclusion

In this paper, we presented an automatic algorithm to generate variable zoom trajectory to maximize magnification in X-ray projection for CT scan of ROI in the sample. The generated trajectory depends on the shape, and dimensions of the whole object, position and dimensions of ROI and CT system geometry. We measured two realistic samples which are challenging for conventional CT measurement due to their flat shape: PCB with BGA and prismatic cell focusing on ROI positioned approximately in the middle of these objects (BGA array and corner of electrode stack). In both cases we were able to achieve higher resolutions, specifically improving defect resolution in solder balls in PCB and resolution of various layers in the electrode stack of the prismatic cell.

To quantify the improvement of resolution we measured MTF from ruby sphere scan and interpolated spatial resolution using bar pattern phantom. With variable zoom trajectory, we were able to achieve up to $5 \times$ higher iSR_{CT} and up to $3 \times$ higher $MTF_{10\%}$ compared to conventional circular scan. The resolution in the reconstructed volume is however directionally dependent. Resolution is higher in directions, which are reconstructed using higher magnification projections. Overall, the resolution depends on the magnification, which is possible to achieve from different directions, which is related to the object's shape and shape and position of the ROI.

Both methods of quantitative evaluation of resolution described in ASTM standard needed to be modified for the scope of this paper, especially due to challenges brought by relatively noisy CT data. There is space for further development of methods, guidelines, and reference objects to characterize spatial resolution in CT data.

Acknowledgements This research was co-financed by the European Union H2020-MSCA-ITN-2020 under grant agreement no. 956172 (xCTing). We also acknowledge CzechNanoLab Research Infrastructure supported by MEYS CR (LM2023051).

Author Contributions PB: writing whole manuscript, concept and design of the work, acquisition and analysis of data. AS: concept and design of the work, acquisition and analysis of data, funding acquisition, supervision. DW: concept and design of the work. TZ: funding acquisition, data acquisition. JK: funding acquisition, supervision. RHS: funding acquisition, supervision. All authors reviewed the manuscript.

Funding Authors received funding from the European Union H2020-MSCA-ITN-2020 under grant agreement no. 956172 (xCTing) and from CzechNanoLab Research Infrastructure supported by MEYS CR (LM2023051).

Data Availability Tomographic slices and related metadata used for quantitative evaluation of resolution were deposited in ZENODO archive: <https://doi.org/10.5281/zenodo.10592077>. Whole tomographic datasets used in this study can be made available upon a reasonable request.

Declarations

Conflict of Interest Pavel Blažek and Alexander Suppes are employees of company Baker Hughes Digital Solutions GmbH. Tomáš Zikmund and Jozef Kaiser are co-owners and members of the Advisory board of company CactuX s.r.o.

Open Access This article is licensed under a Creative Commons Attribution 4.0 International License, which permits use, sharing, adaptation, distribution and reproduction in any medium or format, as long as you give appropriate credit to the original author(s) and the source, provide a link to the Creative Commons licence, and indicate if changes were made. The images or other third party material in this article are included in the article's Creative Commons licence, unless indicated otherwise in a credit line to the material. If material is not included in the article's Creative Commons licence and your intended use is not permitted by statutory regulation or exceeds the permitted use, you will need to obtain permission directly from the copyright holder. To view a copy of this licence, visit <http://creativecommons.org/licenses/by/4.0/>.

References

- Qian, G., Monaco, F., Meng, D., Lee, S.-J., Zan, G., Li, J., Karpov, D., Gul, S., Vine, D., Stripe, B., Zhang, J., Lee, J.-S., Ma, Z.-F., Yun, W., Pianetta, P., Yu, X., Li, L., Cloeten, P., Liu, Y.: The role of structural defects in commercial lithium-ion batteries. *Cell Rep. Phys. Sci.* **2**, 100554 (2021). <https://doi.org/10.1016/j.xcrp.2021.100554>
- de Limé, A.B., Lein, T., Maletti, S., Schmal, K., Reuber, S., Heubner, C., Michaelis, A.: Impact of electrode defects on battery cell performance: a review. *Batter. Supercaps* **5**, e202200239 (2022). <https://doi.org/10.1002/batt.202200239>
- Lall, P., Deshpande, S., Wei, J., Suhling, J.: Non-destructive crack and defect detection in SAC solder interconnects using cross-sectioning and X-ray micro-CT, 2014 IEEE 64th electronic components and technology conference (ECTC) (2014) 1449–1456. <https://doi.org/10.1109/ECTC.2014.6897484>.
- Chanchani, R.: 3D X-ray CT Analysis of solder joints in area array electronic package assemblies, (n.d.). <https://www.osti.gov/servlets/purl/1106308> (Accessed 30 Jan 2024).
- Ranadive, N.: Use of combination 2d and CT scan X-ray imaging for solder joint inspection, in: n.d. https://www.circuitinsight.com/pdf/xray_solder_joint_inspection_smta.pdf.
- Sumimoto, T., Maruyama, T., Azuma, Y., Goto, S., Mondou, M., Furukawa, N., Okada, S.: Detection of defects of BGA by tomography imaging, in: n.d. <https://www.iiisci.org/Journal/pdv/sci/pdfs/P729631.pdf>.
- Villarraga-Gómez, H., Begun, D.L., Bhattad, P., Mo, K., Norouzi Rad, M., White, R.T., Kelly, S.T.: Assessing rechargeable batteries with 3D X-ray microscopy, computed tomography, and nanotomography. *Nondestructive Test. Eval.* **37**, 519–535 (2022). <https://doi.org/10.1080/10589759.2022.2070165>
- Fu, Y., Yao, X.: A review on manufacturing defects and their detection of fiber reinforced resin matrix composites. *Compos. Part C: Open Access* **8**, 100276 (2022). <https://doi.org/10.1016/j.jcocom.2022.100276>
- Huang, X., Zhu, S., Huang, X., Su, B., Ou, C., Zhou, W.: Detection of plated through hole defects in printed circuit board with X-ray. In: 2015 16th international conference on electronic packaging technology (ICEPT), IEEE, Changsha, China, 2015: pp. 1296–1301. <https://doi.org/10.1109/ICEPT.2015.7236817>.
- Christoph, R., Neumann, H.J.: *X-ray Tomography in Industrial Metrology: Precise. Economical and Universal*, Verlag Moderne Industrie (2011)
- Yu, Z., Noo, F., Dennerlein, F., Lauritsch, G., Hornegger, J.: FDK-type reconstruction algorithms for the reverse helical trajectory. In: IEEE nuclear science symposium conference record, 2011, pp. 3980–3985. <https://doi.org/10.1109/NSSMIC.2011.6153757>.
- Yu, Z., Lauritsch, G., Dennerlein, F., Mao, Y., Hornegger, J., Noo, F.: Extended ellipse-line-ellipse trajectory for long-object cone-beam imaging with a mounted C-arm system. *Phys. Med. Biol.* **61**, 1829 (2016). <https://doi.org/10.1088/0031-9155/61/4/1829>
- Kingston, A.M., Myers, G.R., Latham, S.J., Recur, B., Li, H., Sheppard, A.P.: Space-filling X-ray source trajectories for efficient scanning in large-angle cone-beam computed tomography. *IEEE Trans. Comput. Imaging* **4**, 447–458 (2018). <https://doi.org/10.1109/tci.2018.2841202>
- Blažek, P., Guricova, P., Klvac, O., Brinek, A., Kazda, T., Zelenka, F., Zikmund, T., Kaiser, J.: Multiscale 3D analysis of defects and temporal development of electrode morphology in lithium-ion batteries by X-ray computed tomography. *ECS Trans.* **105**, 69–76 (2021). <https://doi.org/10.1149/10501.0069ecst>
- Kingston, A.M., Yang, Q., Grewar, M.G., Delgado-Friedrichs, O., Myers, G.R., Latham, S.J., Sheppard, A.P.: Techniques for high-fidelity X-ray micro-tomography of additively manufactured metal components. *Nondestructive Test. Eval.* **35**, 241–251 (2020). <https://doi.org/10.1080/10589759.2020.1778684>
- Zemek, M.: Method for extending the field of view for X-ray computed tomography with submicron resolution, Brno University of Technology, 2021.
- Herbst, M., Schebesch, F., Berger, M.: Dynamic detector offsets for field of view extension in C-arm computed tomography with application to weight-bearing imaging. *Med. Phys.* **42**, 2718–2729 (2015)
- Industrial CT Scanner, Radiography | Waygate Technologies, (n.d.). <https://www.bakerhughes.com/waygate-technologies/radiography-and-ct-services/system-updates-and-upgrades/software-updates-radiography-ct-0> (Accessed 23 Jan 2024).
- Wood, C.E., O'Brien, N., Denysov, A., Blumensath, T.: Computed laminography of CFRP using an X-Ray cone-beam and robotic sample manipulator systems. *IEEE Trans. Nucl. Sci.* **66**, 655–663 (2019). <https://doi.org/10.1109/TNS.2019.2895910>
- Fisher, S.L., Holmes, D.J., Jørgensen, J.S., Gajjar, P., Behnsen, J., Lionheart, W.R.B.B., Withers, P.J.: Laminography in the lab: imaging planar objects using a conventional x-ray CT scanner. *Meas. Sci. Technol.* **30**, 35401 (2019). <https://doi.org/10.1088/1361-6501/aafcae>
- Delgado-Friedrichs, O., Kingston, A.M., Young, B., Latham, S.J., Myers, G.R., Sheppard, A.P.: A multi-scan refinement technique combining cone-beam tomography and laminography. *Tomogr. Mater. Struct.* **2**, 100012 (2023). <https://doi.org/10.1016/j.tmater.2023.100012>
- Yan, X., Leahy, R.M.M.: Cone beam tomography with circular, elliptical and spiral orbits. *Phys. Med. Biol.* **37**, 493–506 (1992)
- Dabravolski, A., Batenburg, K.J., Sijbers, J.: Adaptive zooming in X-ray computed tomography. *J. Xray Sci. Technol.* **22**, 77–89 (2014). <https://doi.org/10.3233/XST-130410>
- Nikishkov, Y., Kuksenko, D., Makeev, A.: Variable zoom technique for X-Ray computed tomography. *NDT E Int.* (2020). <https://doi.org/10.1016/j.ndteint.2020.102310>
- FF85 CT - Comet Yxlon, (n.d.). <https://yxlon.comet.tech/en/products/ff85-ct> (Accessed 30 Dec 2023).
- ASTM E (2006) 1695–95 Standard test method for measurement of computed tomography (CT) system performance, (n.d.).
- E07 Committee, ASTM E2576. Practice for manufacturing characterization of digital detector arrays, (n.d.). https://doi.org/10.1520/E2597_E2597M-14.
- Narukawa, Y., Ooka, N., Makihara, Z., Nemoto, Y., Yokota, K.: Need for training on how to use the image quality indicators in education of digital radiography, in: Singapore, n.d. <http://www.ndt.net/?id=22162>.

Publisher's Note Springer Nature remains neutral with regard to jurisdictional claims in published maps and institutional affiliations.